Mineralogy and Petrology (2021) 115:283–297
https://doi.org/10.1007/s00710-021-00743-1

ORIGINAL PAPER

Evolution of spinel-bearing ultrahigh-temperature granulite in the Jining complex, North China Craton: constrained by phase equilibria and Monte Carlo methods

Bin Wang[1] · Chun-Jing Wei[1] · Wei Tian[1]

Received: 3 November 2020 / Accepted: 10 February 2021 / Published online: 25 February 2021

Abstract

The peak temperature and timescale of ultrahigh-temperature (UHT) metamorphism are significant for understanding its thermal budget and geodynamic evolution. The spinel-bearing (sapphirine-absent) UHT granulite at the Xuwujia area in the Jining complex, North China Craton was revealed to have undergone a metamorphic evolution that involves the pre-T_{max} (maximum temperature) heating decompression to the T_{max} stage with an extreme temperature of ~1125 °C, the post-T_{max} cooling to the fluid-absent solidus (~860 °C) at 0.8–0.9 GPa, and sub-solidus decompression. The T_{max} condition was recorded by the inferred feldspar-absent peak assemblage of spinel ± garnet. The post-T_{max} cooling evolution was indicated by the sequential appearances of plagioclase, K-feldspar, sillimanite and biotite, as well as the core-to-rim ascending grossular component in garnet. Moreover, some texturally zoned spinel has exsolved lamellae of magnetite in the core and shows rim-ward increase of Mg and Al, which suggests a temperature decrease from >1100 °C in local domains isolated from quartz. Spinel with exsolved magnetite lamellae or low $Al/(Al + Fe^{3+})$ is therefore proposed as an indicator for UHT conditions in metapelites. Probability simulation on the collected zircon ages yields a timescale of ~40 Myr (95% confidence; during 1.90–1.94 Ga) for the supra-solidus cooling stage of the UHT metamorphism in the Jining complex. This extreme UHT metamorphism has reached the rock's dry solidus (~1125 °C) and undergone slow cooling, which is interpreted to result from a post-orogenic plume activity with sufficient advective heating from hyperthermal mafic intrusions.

Keywords Spinel · Pelitic granulite · Timescale · Ultrahigh-temperature metamorphism · Jining complex

Introduction

UHT metamorphism in pelitic rocks is identified by diagnostic mineral assemblages, such as sapphirine plus quartz and orthopyroxene plus sillimanite (e.g. Harley 2008; Kelsey 2008). The spinel plus quartz assemblage is widely reported in UHT metapelites worldwide, but is commonly regarded to be non-diagnostic for UHT metamorphism (e.g. Harley 2008), because its stability range can be influenced by the incorporation of elements such as Zn and Cr (Nichols et al. 1992; Guiraud et al. 1996). Nevertheless, spinel plus quartz assemblage is a possible UHT advocate when spinel has exsolved lamellae of ferrotitanium oxides or directly contacts with them, because in these cases, spinel can be miscible with magnetite, ulvöspinel and so on (e.g. Kelsey 2008; Clarke et al. 1989; Waters 1991; Sengupta et al. 1999). For example, spinel with exsolved titanomagnetite in granulites from the Eastern Ghats was reported to record metamorphic temperatures of 1060–1140 °C (Das et al. 2017). On this account, spinel compositions and exsolution behaviour may be useful for constraining the temperatures of UHT metamorphism, but this potential is insufficiently investigated. Moreover, the enlargement of spinel stability field caused by elements, such as Zn and Cr, may be insignificant if their contents are very low. The factors that primarily influence the stability of spinel also need to be addressed.

UHT granulites in the Jining complex, Khondalite Belt, North China Craton (NCC) have attracted much attention in the last decade. Most of these UHT granulites are characterized by spinel-bearing (sapphirine-absent) assemblages such

Editorial handling: S. W. Faryad

✉ Chun-Jing Wei
cjwei@pku.edu.cn

[1] MOE Key Laboratory of Orogenic Belts and Crustal Evolution, School of Earth and Space Sciences, Peking University, Beijing 100871, China

as that in the Xuwujia area. The peak temperatures of the spinel-bearing granulite therein were estimated as ~1120 °C by the occurrence of ferro-pseudobrookite (Wang et al. 2019) at odds with ~1020 °C determined by two-feldspar thermometry (Jiao and Guo 2011) and above 960 °C by phase equilibria modelling (Li and Wei 2018; Huang et al. 2019). As peak temperature is crucial for evaluating the heat budget and understanding the geodynamic nature of UHT metamorphism, more data are required to resolve the discrepant estimates of peak temperature. On the other hand, an almost uniform mean age of ~1.92 Ga for the UHT metamorphism in the Jining complex was widely reported based on zircon U–Pb dating (Santosh et al. 2007a; Li and Wei 2018; Lobjoie et al. 2018; Li et al. 2019), but the mean age was obtained from wide and continuous age spans on the concordia curve and its geological meaning is ambiguous. Seeing that UHT metamorphism with post-peak slow cooling (generally >30 Myr) or fast cooling (mostly <10 Myr) was interpreted to have formed in distinct tectonic regimes (e.g. Kelsey and Hand 2015; Harley 2016), Wang et al. (2020) constrained a duration of ~40 Myr for supra-solidus cooling stage of the UHT metamorphism. As this outcome is based on dating of a single sapphirine-bearing sample, its universality and internal consistency still need an assessment.

The present study will focus on three targets. They are: (i) to retrieve the metamorphic evolution especially the peak temperatures of the spinel-bearing (sapphirine-absent) granulite in the Xuwujia area using phase equilibria modelling, (ii) to address the stability and compositional variation of spinel during UHT metamorphism, and (iii) to assess or authenticate the

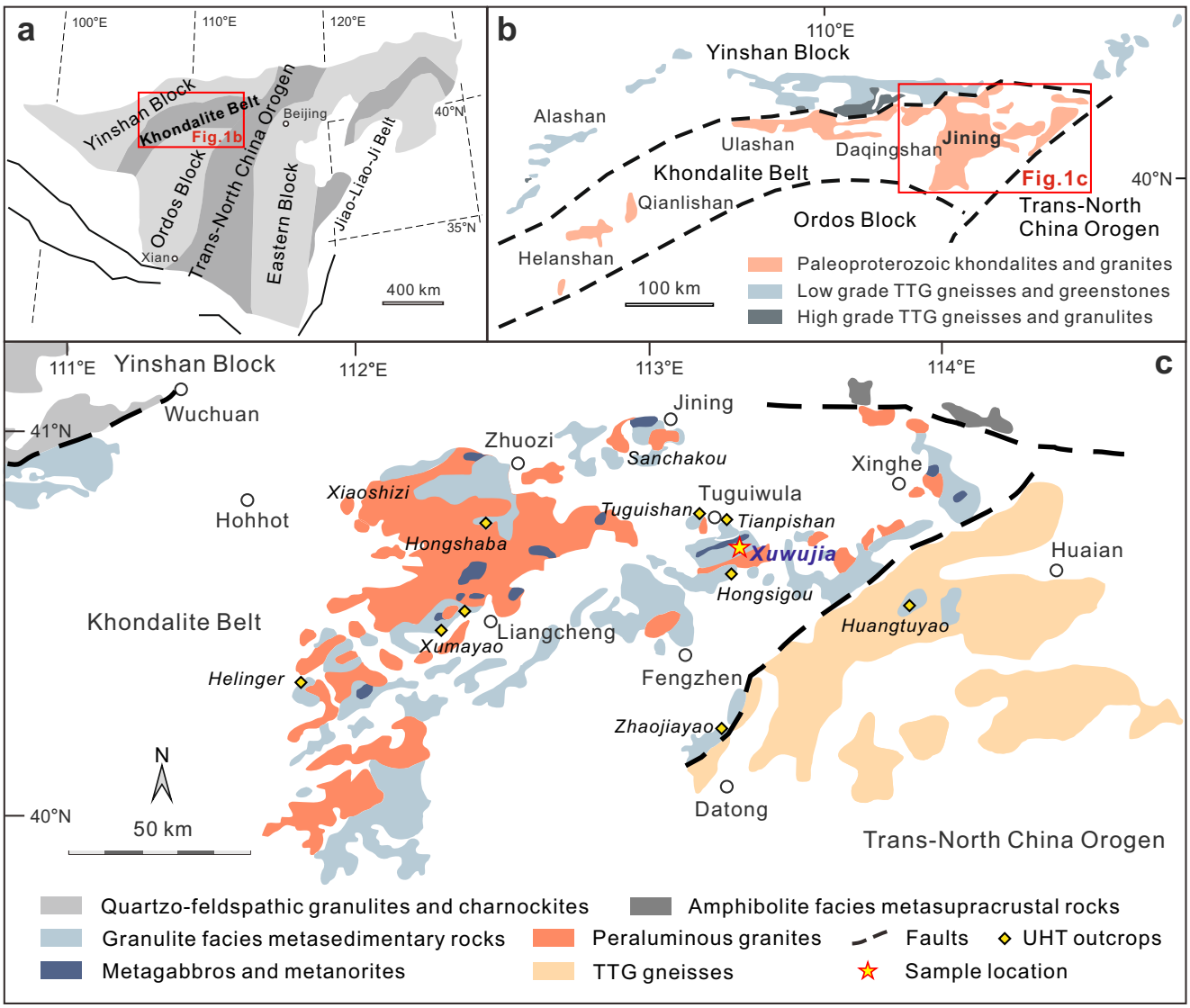

Fig. 1 Geologic sketch maps. **a** Tectonic sketch of the North China Craton (after Zhao et al. 2005). **b** Geologic sketch showing the distribution of the Khondalite Belt and its sub-units (after Zhao et al. 2005). **c** Geologic map of the Jining complex (modified after Guo et al. 1999), showing the lithologic distribution and the localities of UHT granulites

timescale of the UHT metamorphism in the Jining complex using Monte Carlo simulation.

Geologic setting

The Khondalite Belt in the NCC was regarded to result from the collision between the southern Ordos Block and the northern Yinshan Block at ~1.95 Ga (Fig. 1a, b; e.g. Zhao et al. 2005, 2012). It exposes in the Helanshan–Qianlishan, Daqingshan–Ulashan and Jining areas from west to east (Fig. 1b). Recent studies suggest that the Khondalite Belt may extend southward as the basement beneath the Ordos Block (Wang et al. 2014, 2017) and eastward to the Huaian complex (Zhai and Santosh 2011; Zhou et al. 2017; Liao and Wei 2019).

The Jining complex is the eastern segment of the Khondalite Belt, where the lithology is dominated by pelitic granulite/gneiss, peraluminous granite and minor meta-gabbronorite (Fig. 1b, c). A growing body of pelitic granulites were reported to record UHT conditions, most of them containing spinel and just a few containing sapphirine (e.g. Liu and Li 2007; Santosh et al. 2007b; Jiao and Guo 2011; Zhang et al. 2012; Liu et al. 2012; Shimizu et al. 2013; Yang et al. 2014; Li and Wei 2016, 2018; Lobjoie et al. 2018; Li et al. 2019). Metamorphic zircon in the UHT granulite yields mean ages of 1.91–1.92 Ga (Santosh et al. 2007a; Li and Wei 2018; Lobjoie et al. 2018; Li et al. 2019) and ~ 1.88 Ga (Yang et al. 2014). The *P*–*T* path for the UHT metamorphism was initially inferred to be anticlockwise with a pressure increase at the pre-T_{max} stage (Santosh et al. 2009; Liu et al. 2011; Shimizu et al. 2013), while was corrected to be clockwise with heating and decompression at the pre-T_{max} stage (Yang et al. 2014; Li and Wei 2016, 2018; Lobjoie et al. 2018; Li et al. 2019). The peraluminous granites commonly contain voluminous garnet, and display crystallization ages of 1.94–1.90 Ga (Zhong et al. 2007; Wang et al. 2018; Huang et al. 2019). They are regarded to relate with extensive anatexis of the metapelites (Shi et al. 2018; Wang et al. 2018). The meta-gabbronorite crystallized at 1.96–1.92 Ga (~1.93 Ga), and metamorphosed at ~1.86 Ga (Peng et al. 2010).

Samples and methods

Sample collection and preparation

The samples in this study were collected from the Xuwujia outcrop (Fig. 1c). The rocks are migmatites with schlieren, comprising felsic leucosomes and mafite-rich mesosomes (Fig. 2a), which reflects extensive melting during high-grade metamorphism (also see Jiao and Guo 2011; Li and Wei 2018). A representative spinel-bearing (sapphirine-absent) pelitic granulite sample 15XWJ02 from the mesosomes was selected for petrologic analyses. The sample was trimmed away from stale portions and surface contaminants to prepare thin-sections in thicknesses of 0.02–0.03 mm. The thin-sections were carbon coated for electric conduction in electron probe micro-analyser (EPMA) work.

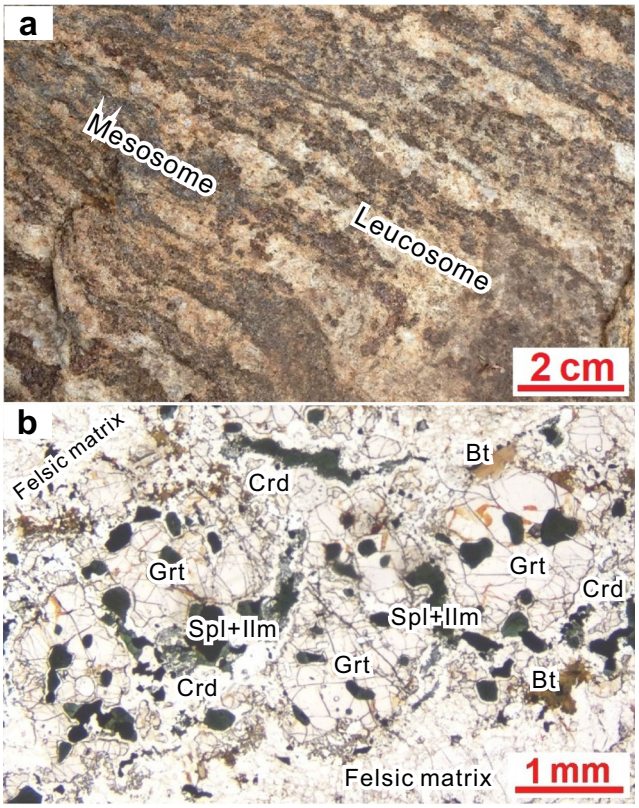

Fig. 2 **a** Photograph showing the field occurrence of UHT granulite at the Xuwujia area (Li and Wei 2018). **b** Photograph showing the texture of the spinel-bearing granulite sample 15XWJ02

Mineral analyses

Analyses for the chemical compositions of minerals were performed by means of a JEOL-8230 EPMA. The system was operated in wavelength-dispersive X-ray spectrometry mode, with an acceleration voltage of 15 kV and a beam current of 10 nA. For all elements, the Kα line has been utilized. The beam was focused to a diameter of 1–2 μm (10 μm for densely and tinily exsolved spinel mantle), and counting times were 10–15 s. The following reference materials [from the "53 minerals standards for microanalysis" set provided by Structure Probe Inc. (SPI) Supplies, West Chester, PA] were used for calibration: sanidine for K, diopside for Ca and Mg, rutile for Ti, jadeite for Na, Al and Si, chromium oxide for Cr, rhodonite for Mn, hematite for Fe, and nickel silicide for Ni. Data were reduced using the PAP (Phi-Rho-Z) correction method (Pouchou and Pichoir 1985). More analytical details

Table 1 Simplified stoichiometric formulae of mineral models used for phase equilibria modelling

Minerals	Formulae
Biotite	$K[Mg_{(1-x)(1-f-y-t)-2/3Q}Fe_{x(1-f-y-t)+2/3Q}Fe^{3+}_{f}Al_{y}Ti_{t}][Mg_{1-x+Q/3}Fe_{x-Q/3}]_2[Al_{1+f+y}Si_{3-f-y}]O_{10+2t}(OH)_{2-2t}$
Cordierite	$[Mg_{1-x}Fe_{x}]_2Al_4Si_5O_{18-h}(OH)_{2h}$
Feldspars	$[K_{y(1-x)}Na_{(1-y)(1-x)}Ca_{x}][Al_{1+x}Si_{3-x}]O_8$
Garnet	$[Ca_{z}Mg_{(1-z)(1-x)}Fe_{(1-z)x}]_3[Fe^{3+}_{f}Al_{1-f}]_2Si_3O_{12}$
Ilmenite	$[Fe_{(x+Q)/2}Ti_{(x-Q)/2}Fe^{3+}_{1-x}][Fe_{(x-Q)/2}Ti_{(x+Q)/2}Fe^{3+}_{1-x}]O_3$
Spinel	$[Mg_{1-x}Fe_{x}]_{1+t}[Fe^{3+}_{1-y}Al_{y}]_{2-2t}Ti_{t}O_4$

were described elsewhere (Li et al. 2018). The image analyses for exsolved lamellae were performed using ImageJ software, to reintegrate pre-exsolved homogeneous mineral compositions. The area proportions were measured by particles summation. The mass densities used to calculate weight fractions of exsolved lamellae were 5.20 g/cm^3 for magnetite,

Table 2 Chemical compositions (EPMA results) and calculated formulae for minerals in sample 15XWJ02

Constituent	Grt c	Grt r	Spl in	Spl sy	Spl c, oc	Spl c, el	Spl m	Spl r	Perthite r, oc	Perthite c, oc	Perthite c, el	Pl	Pl in	Bt	Crd	Opx
Major oxides (wt%)																
SiO_2	38.76	38.87	–	–	–	–	–	–	64.63	66.27	58.02	59.07	58.24	36.92	50.22	50.99
TiO_2	–	–	0	0	0.01	0.15	0	0.05	–	–	–	–	–	5.64	–	–
Al_2O_3	21.66	21.18	59.24	60.51	57.25	0.41	54.08	56.68	18.34	18.56	26.01	25.54	26.34	13.49	33.25	4.41
Cr_2O_3	–	–	0.29	0.66	0.37	0.19	0.35	0.39	–	–	–	–	–	–	–	–
FeO	27.07	26.98	30.91	26.67	29.77	90.37	34.13	30.02	–	–	–	–	–	13.63	4.09	21.77
MnO	0.55	0.52	0.11	0.03	0.06	0	0.07	0.05	–	–	–	–	–	0.04	0.04	0.23
MgO	10.65	9.95	8.87	11.74	9.62	0.06	9.13	9.66	–	–	–	–	–	14.82	11.77	22.17
NiO	–	–	0.04	0.17	0.19	0.06	0.06	0.06	–	–	–	–	–	–	–	–
CaO	1.23	1.49	–	–	–	–	–	–	0.17	0.47	8.1	7.76	8.4	–	–	0.07
Na_2O	–	–	–	–	–	–	–	–	1.71	1.97	5.83	6.71	6.3	0.11	–	–
K_2O	–	–	–	–	–	–	–	–	13.44	12.61	0.8	0.18	0.15	9.36	–	–
Total	99.92	98.99	99.46	99.78	97.27	91.24	97.82	96.91	98.29	99.88	98.76	99.26	99.43	94.01	99.37	99.64
Calculated mineral formulae (apfu)																
O*	12	12	4	4	4	4	4	4	8	8	8	8	8	11	18	6
Si	2.97	3.01	–	–	–	–	–	–	3.00	3.02	2.62	2.65	2.61	2.79	5.01	1.89
Ti	–	–	0.00	0.00	0.00	0.00	0.00	0.00	–	–	–	–	–	0.32	–	–
Al	1.95	1.93	1.92	1.91	1.89	0.02	1.80	1.88	1.01	1.00	1.39	1.35	1.39	1.20	3.91	0.19
Cr	–	–	0.01	0.01	0.01	0.01	0.01	0.01	–	–	–	–	–	–	–	–
Fe^{3+}	0.12	0.04	0.08	0.07	0.10	1.97	0.19	0.11	–	–	–	–	–	0.00	0.07	0.02
Fe^{2+}	1.61	1.71	0.63	0.53	0.59	1.00	0.61	0.59	–	–	–	–	–	0.86	0.28	0.66
Mn	0.04	0.03	0.00	0.00	0.00	0.00	0.00	0.00	–	–	–	–	–	0.00	0.00	0.01
Mg	1.21	1.15	0.36	0.47	0.40	0.00	0.38	0.40	–	–	–	–	–	1.67	1.75	1.23
Ni	–	–	0.00	0.00	0.00	0.00	0.00	0.00	–	–	–	–	–	–	–	–
Ca	0.10	0.12	–	–	–	–	–	–	0.01	0.02	0.39	0.37	0.40	–	–	0.00
Na	–	–	–	–	–	–	–	–	0.15	0.17	0.51	0.58	0.55	0.02	–	–
K	–	–	–	–	–	–	–	–	0.80	0.73	0.05	0.01	0.01	0.90	–	–
Σ cations	8	8	3	3	3	3	3	3	5.0	4.9	5.0	5.0	5.0	7.8	11	4
X(phase)	0.43	0.40	0.36	0.47	0.40	0.00	0.39	0.41	0.01	0.02	0.41	0.39	0.42	0.66	0.86	0.65
Y(phase)	0.03	0.04	0.96	0.96	0.95	0.01	0.90	0.94	0.83	0.79	0.05	0.01	0.01			

c core; *m* mantle; *r* rim; *in* mineral inclusions; *sy* symplectite; *oc* oikocryst; *el* exsolved lamella

$X(Grt/Spl/Bt/Crd/Opx) = X_{Mg} = Mg/(Mg + Fe^{2+})$; $X(Perthite/Pl) = X_{an} = Ca/(Ca + Na + K)$; $Y(Grt) = X_{gr} = Ca/(Mg + Fe^{2+} + Ca + Mn)$; $Y(Spl) = X_{Al} = Al/(Al + Fe^{3+} + Cr)$; $Y(Perthite/Pl) = X_{or} = K/(Ca + Na + K)$

– Below detection limit or not analyzed

* Assumed number of oxygen atoms per formula unit

3.55 g/cm^3 for spinel, 2.67 g/cm^3 for plagioclase and 2.57 g/cm^3 for K-feldspar. Mineral formulae and site occupancies were determined based on assumed fixed oxygen amounts per formula unit, with trivalent iron calculated by stoichiometric charge balance.

Calculations

The model system NCKFMASHTO (Na_2O–CaO–K_2O–FeO–MgO–Al_2O_3–SiO_2–H_2O–TiO_2–Fe_2O_3) was chosen for phase equilibria modelling. The calculations were performed

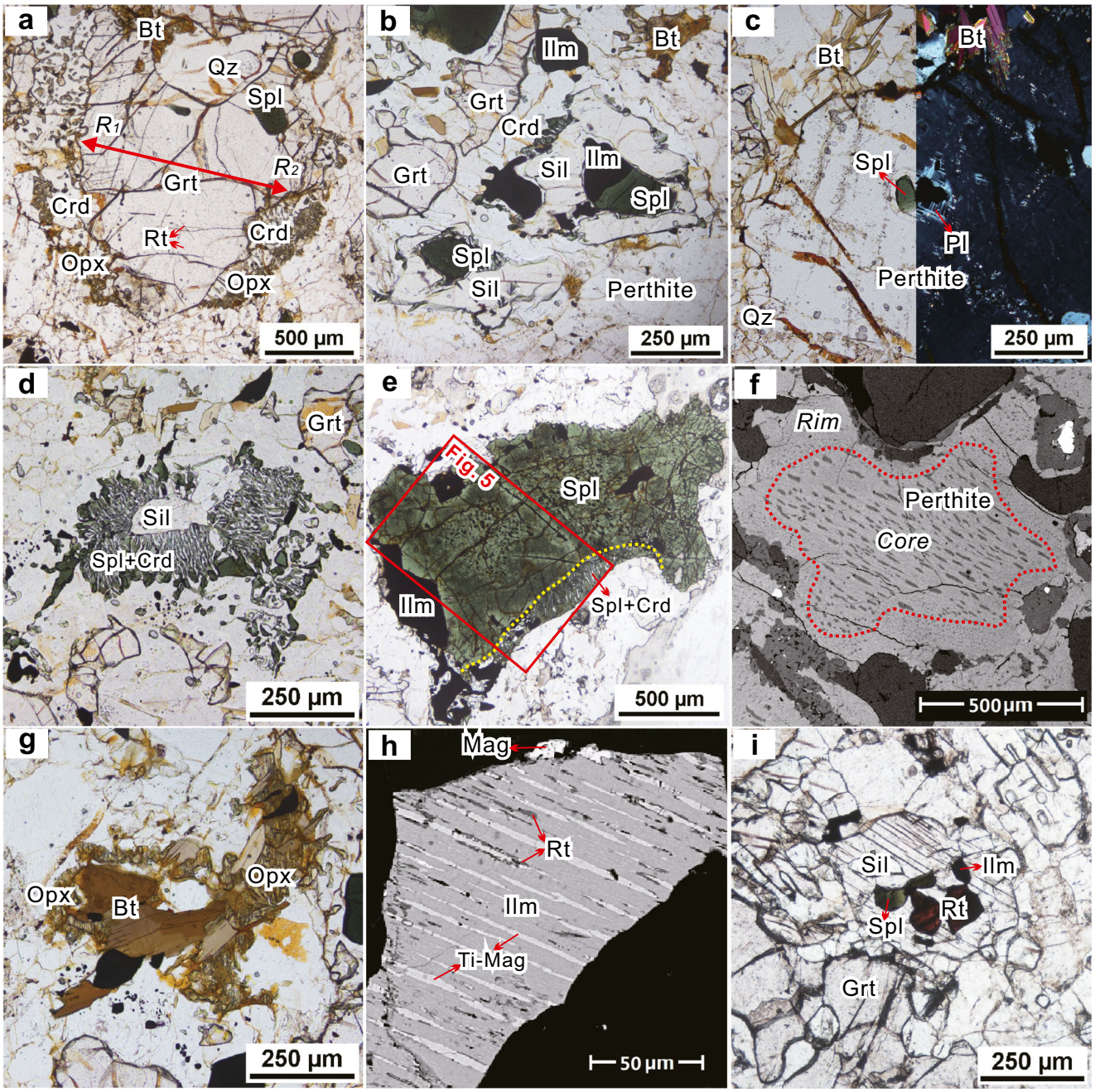

Fig. 3 Photomicrographs and BSE images of minerals and textures in sample 15XWJ02. **a** Garnet contains spinel inclusions in its rim domain and is surrounded by the symplectite of orthopyroxene plus cordierite. **b** Sillimanite overgrows around the intergrown spinel and ilmenite, and develops cordierite coronae locally. **c** Perthite contains inclusions of spinel and plagioclase, and biotite flakes are aggregated around perthite. **d** Symplectite of spinel plus cordierite replaces sillimanite. **e** Some coarse spinel grains display zoning texture. **f** A perthite grain shows dense exsolution lamellae in the core and sparse exsolution spots in the rim. **g** Orthopyroxene overgrows around biotite flakes. **h** Ilmenite contains mottles of rutile, magnetite overgrows around ilmenite, and titanomagnetite parallelly exsolves in ilmenite. **i** Sillimanite has inclusions of spinel, rutile and ilmenite. Abbreviations of mineral names after Whitney and Evans (2010)

using THERMOCALC 3.40 (Powell and Holland 1988) with dataset ds62 (Holland and Powell 2011). Mineral activity–composition relationships are the same as those in White et al. (2014) and references therein, with simplified stoichiometric formulae shown in Table 1. The bulk-rock composition was taken from Wang et al. (2019) and normalized in the model system. The H_2O content was adjusted to ensure the final-phase assemblage occurring just above the solidus (e.g. Korhonen et al. 2011, 2012), where hydrous mineral (biotite) is in the observed mode (around 3–5 wt%). The Fe^{3+}/Fe value was properly adjusted using T–X_{Fe}^{3+} diagram (see further below), ensuring that ilmenite occurs as the predominant phase of Ti − Fe oxide, and the reintegrated Fe^{3+} content in spinel can be reproduced further along the path.

As a large quantity of zircon age data for UHT granulites in the Jining complex have been accumulated, the Monte Carlo simulation (a probability simulation) was performed to constrain the duration of the UHT metamorphism, because this method can avoid the statistical bias resulted from taking all dates into account and can well define an accurate and credible timescale of geologic events (e.g. Svensen et al. 2012). We collected 260 zircon $^{207}Pb/^{206}Pb$ dates for the UHT granulite/gneiss (Santosh et al. 2007a; Yang et al. 2014; Li and Wei 2016, 2018; Lobjoie et al. 2018; Li et al. 2019). Among them, 86 dates were rejected through 12 times of iterative consistency check, which include those with abnormally large deviations and those recognized to be outliers. We generated 50,000 simulations of the duration. In each simulation, two random ages from the rest 174 data are assigned to calculate an age difference.

Results

Petrography and mineral chemistry

The spinel-bearing UHT granulite consists of quartz (Qz), perthite, plagioclase (Pl), garnet (Grt), sillimanite (Sil), spinel (Spl), orthopyroxene (Opx), biotite (Bt), cordierite (Crd) and Ti − Fe oxides (abbreviations of mineral names after Whitney and Evans 2010). Garnet and spinel with subordinate biotite and cordierite are randomly distributed in the felsic matrix (Fig. 2b). Representative results of chemical analyses of minerals are presented in Table 2.

Garnet occurs in variable size of 0.2–1.5 mm across. It is surrounded by a symplectite of orthopyroxene plus cordierite, and has spinel inclusions limited to its rim domains (Fig. 3a). It also includes exsolved rutile needles oriented in three directions (Fig. 3a). Garnet contains X_{alm} of 0.54–0.57, X_{prp} of 0.39–0.42, X_{sps} of ~0.01 and X_{gr} of 0.03–0.04 (where $X_{alm} = Fe^{2+}/(Fe^{2+}+Mg+Ca+Mn)$, $X_{prp} = Mg/(Fe^{2+}+Mg+Ca+Mn)$, $X_{sps} = Mn/(Fe^{2+}+Mg+Ca+Mn)$ and $X_{gr} = Ca/(Fe^{2+}+$

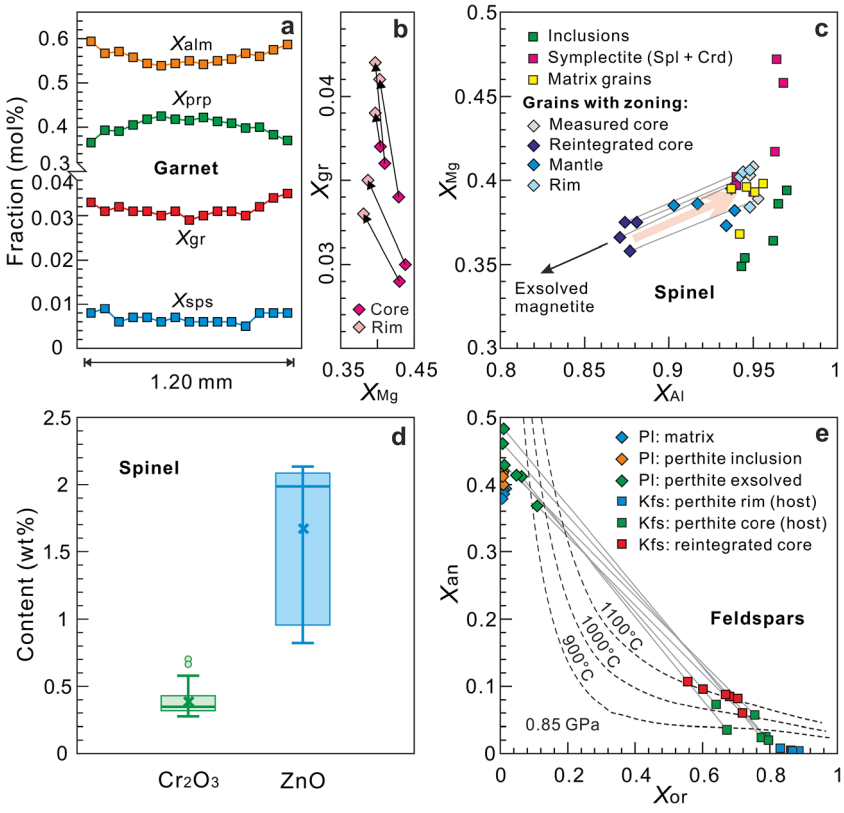

Fig. 4 Mineral compositional diagrams. **a** Zoning profiles of X_{alm}, X_{prp}, X_{gr} and X_{sps} for garnet. **b** X_{gr}–X_{Mg} diagram showing the compositional variation from core to rim in garnet. **c** X_{Mg}–X_{Al} diagram showing the compositional variation and zoning characteristic of spinel. **d** Box plots of Cr_2O_3 and ZnO contents for spinel (Data of ZnO are from Li and Wei (2018), Li (2019) and Wang et al. (2019)). **e** X_{an}–X_{or} diagram for measured perthite, plagioclase and reintegrated K-feldspar, with isotherms at 0.85 GPa based on the models of Elkins and Grove (1990). $X_{alm} = Fe^{2+}/(Fe^{2+}+Mg+Ca+Mn)$; $X_{prp} = Mg/(Fe^{2+}+Mg+Ca+Mn)$; $X_{sps} = Mn/(Fe^{2+}+Mg+Ca+Mn)$; $X_{gr} = Ca/(Mg+Fe^{2+}+Ca+Mn)$; $X_{Mg} = Mg/(Mg+Fe^{2+})$; $X_{Al} = Al/(Al+Fe^{3+}+Cr)$; $X_{an} = Ca/(Ca+Na+K)$; $X_{or} = K/(Ca+Na+K)$

Mg + Ca + Mn)) in the cores, while X_{alm} of 0.57–0.59, X_{prp} of 0.37–0.38 and very similar X_{sps} and X_{gr} in the rims. It shows conspicuous core-to-rim zoning of increasing X_{gr} and X_{alm} but decreasing X_{prp} (Fig. 4a, b). X_{sps} shows an increase in the rim.

Spinel generally coexists with Ti − Fe oxides, and occurs as inclusions in garnet, sillimanite and feldspars (Fig. 3a–c), as symplectite with cordierite surrounding sillimanite (Fig. 3b, d), or as single grains in the matrix. The different types of spinel show similar X_{Al} [= Al/(Al + Fe^{3+}+Cr)) of 0.93–0.96 but variable X_{Mg} (= Mg/(Mg + Fe^{2+})] of 0.35–0.39 in the inclusions, 0.39–0.47 in the symplectites and 0.37–0.40 in the matrix grains (Fig. 4c). Occasionally, some coarse grains in the matrix are zoned, with wide trellised exsolution lamellae of magnetite in the core, very tiny magnetite lamellae in the mantle and lamellae-free in the rim (Figs. 3e and 5). Image analyses suggest that magnetite lamellae occupy 6.9–7.8 vol% of the core domains, allowing reintegrated compositions with X_{Al} of 0.87–0.88 and X_{Mg} of 0.36–0.38 (Fig. 4c), distinct from the measured host compositions with X_{Al} of 0.93–0.95 and X_{Mg} of 0.39–0.41. The measured compositions show X_{Al} of 0.90–0.94 and X_{Mg} of 0.37–0.39 in the mantle, and X_{Al} of ~0.94 and X_{Mg} of 0.38–0.41 in the rim. That is, these zoned spinel grains are characteristic of increasing X_{Al} from core to rim (Fig. 4c). Moreover, spinel contains Cr_2O_3 of 0.27–0.70 wt% and ZnO of 0.82–2.14 wt% (Fig. 4d), with X_{Cr} [= Cr/(Al + Fe^{3+}+Cr)] below ~0.01 and X_{Zn} [= Zn/(Mg + Fe^{2+}+ Zn)] of 0.02–0.05.

Sillimanite occurs as overgrowths commonly surrounding spinel and ilmenite (Fig. 3b). Sillimanite itself is surrounded by symplectite of spinel plus cordierite (Fig. 3d).

Perthite occurs as anhedral grains of 0.5–1.5 mm across, and occasionally has inclusions of plagioclase and spinel (Fig. 3c). It shows dense exsolution lamellae in the core and sparse exsolution spots in the rim (Fig. 3f). In the core domain, the exsolution lamellae are 5–10 μm wide and occupy 6.1–17.6 vol% by image analyses. Therein, the host sanidine has X_{or} [= K/(Ca + Na + K)] of 0.64–0.80 and X_{an} [= Ca/(Ca + Na + K)] of 0.02–0.07, and the lamellae have X_{an} of 0.37–0.48 and X_{or} of 0.01–0.11, which allows reintegrating a supra-solvus K-feldspar (Kfs) with X_{or} of 0.56–0.72 and X_{an} of 0.06–0.11 (Fig. 4e). In the rim domain, the host sanidine has X_{or} of 0.83–0.89 and X_{an} below 0.01, while the exsolved spots are too small to be analyzed.

Plagioclase occurs as anhedral crystals with variable sizes of 0.1–1 mm. It occasionally displays as inclusions in perthite or contains inclusions of spinel (Fig. 3c). Matrix plagioclase has X_{an} of 0.38–0.39, but the grains enclosed in perthite have slightly higher X_{an} of 0.40–0.42 (Fig. 4e).

Biotite occurs as aggregated flakes with irregular and cuspate boundaries in the matrix (Fig. 3a–c, g), commonly surrounding garnet or perthite and occasionally surrounded by orthopyroxene. It shows noticeable TiO_2 contents of 4.55–5.64 wt%, and X_{Mg} of 0.65–0.69.

Cordierite occurs as coronae or symplectite with orthopyroxene (around garnet) or spinel (around sillimanite; Fig. 3a–d). It has a uniform composition with X_{Mg} of 0.86–0.88.

Orthopyroxene occurs as symplectite with cordierite around garnet (Fig. 3a) or overgrows around biotite (Fig. 3g). It contains Al_2O_3 of 3.41–5.48 wt% and X_{Mg} of 0.63–0.66.

Ti − Fe oxides are mainly ilmenite (Ilm) with small amounts of rutile (Rt), magnetite (Mag) and titanomagnetite (Ti-Mag). Ilmenite contains exsolved lamellae of titanomagnetite and mottles of rutile along the titanomagnetite boundaries (Fig. 3h), which may imply the formation of tiny rutile during the redox exsolution of titanomagnetite through open system precipitation (Wang et al. 2019; Proyer et al. 2013). Magnetite occurs as exsolutions in spinel (Figs. 3e and 5) and as overgrown rims around ilmenite (Fig. 3h), indicating its later formation. Titanomagnetite occurs as 5–10 μm wide parallel exsolution lamellae in ilmenite (Fig. 3h). Rutile occurs as inclusions in sillimanite (Fig. 3i) and as mottles in ilmenite.

Based on the textural relationships described above, the peak assemblage is inferred to include silicate melt (Liq) and spinel likely together with garnet, and the post-peak evolution

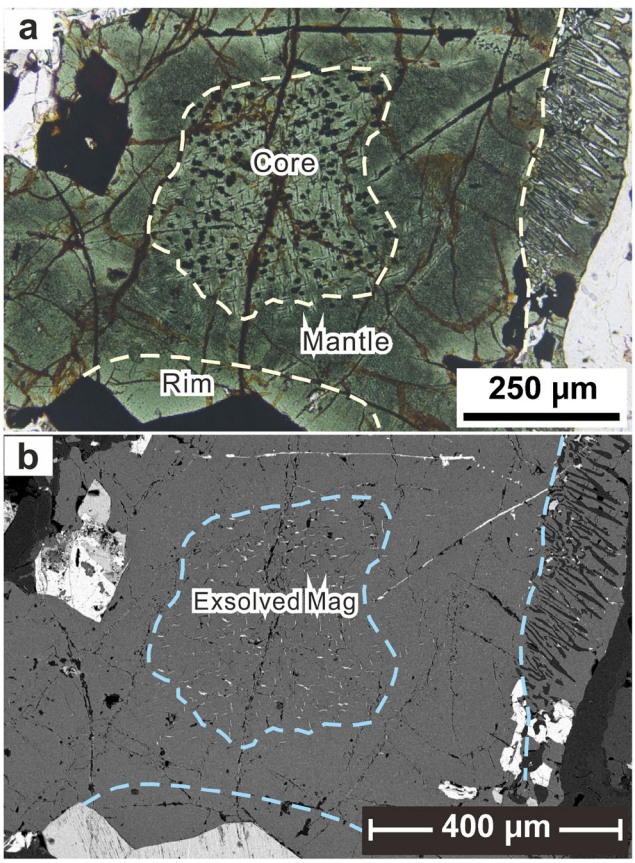

Fig. 5 Zoning texture of the spinel. Photomicrograph (**a**) and BSE image (**b**) showing the wider trellised exsolution lamellae of magnetite in the core, very tiny magnetite lamellae in the mantle and lamellae-free rim

may involve the sequential appearance of plagioclase, perthite, biotite and the symplectitic or coronary assemblages of cordierite, orthopyroxene and spinel (Fig. 3a–d, g). Sillimanite should be absent in the peak assemblage and formed before biotite, probably growing together with the feldspars (Fig. 3b, c).

Phase equilibria

Pressure–temperature evolution

A *P*–*T* pseudosection for sample 15XWJ02 was calculated over 0.4–1.2 GPa and 750–1200 °C (Fig. 6a). It is contoured with the X_{an}(Kfs), X_{an}(Pl), X_{gr}(Grt) and X_{Al}(Spl) isopleths for the relevant assemblages. The inferred peak assemblage including spinel and garnet is modelled to be stable at temperatures over ~1125 °C at 0.8–0.9 GPa, covering the rock's dry solidus (~1125 °C at 0.8–0.9 GPa; Fig. 6a). The observed post-peak sequential appearance of plagioclase, perthite/sillimanite and biotite is well consistent with the cooling evolution at pressures of 0.8–0.9 GPa. It includes (i) the formation of plagioclase plus quartz at ~1125 °C followed by K-feldspar at ~1110 °C, as a result of the crystallization of unsegregated melts (Fig. 6b); (ii) the growth of sillimanite and garnet at the expense of spinel and quartz (Spl + Qz = Grt + Sil; R1 in Fig. 6b) from ~1110 °C to ~1085 °C, accompanied with further melt crystallization; and (iii) the growth of biotite at the expense of melt, garnet and K-feldspar (Grt + Kfs + Liq = Bt + Sil + Pl + Qz; R2 in Fig. 6b) from ~870 °C to the fluid-absent solidus. Along the cooling process, the substantial melt crystallization that consumes over 80% melts (60 to 10 mol%) occurs at 1030–1110 °C (C in Fig. 6b). The above metamorphic evolution can be well supported by the contours of mineral compositions. The reintegrated X_{Al} = 0.87–0.88 in the core of the zoned spinel can yield temperatures of ~1150 °C in the peak assemblage (Grt − Spl − Liq) or 1090–1100 °C in the sillimanite-bearing assemblage (Grt − Sil − Kfs − Pl − Qz − Spl − Liq). The reintegrated perthite composition with X_{an} = 0.06–0.10 yields temperatures above 1075 °C, in accordance with the voluminous growth of K-feldspar (Fig. 6). The core-to-rim X_{gr} increasing (0.03 → 0.04) in garnet indicates a cooling trend with a wide temperature range at 900–1100 °C

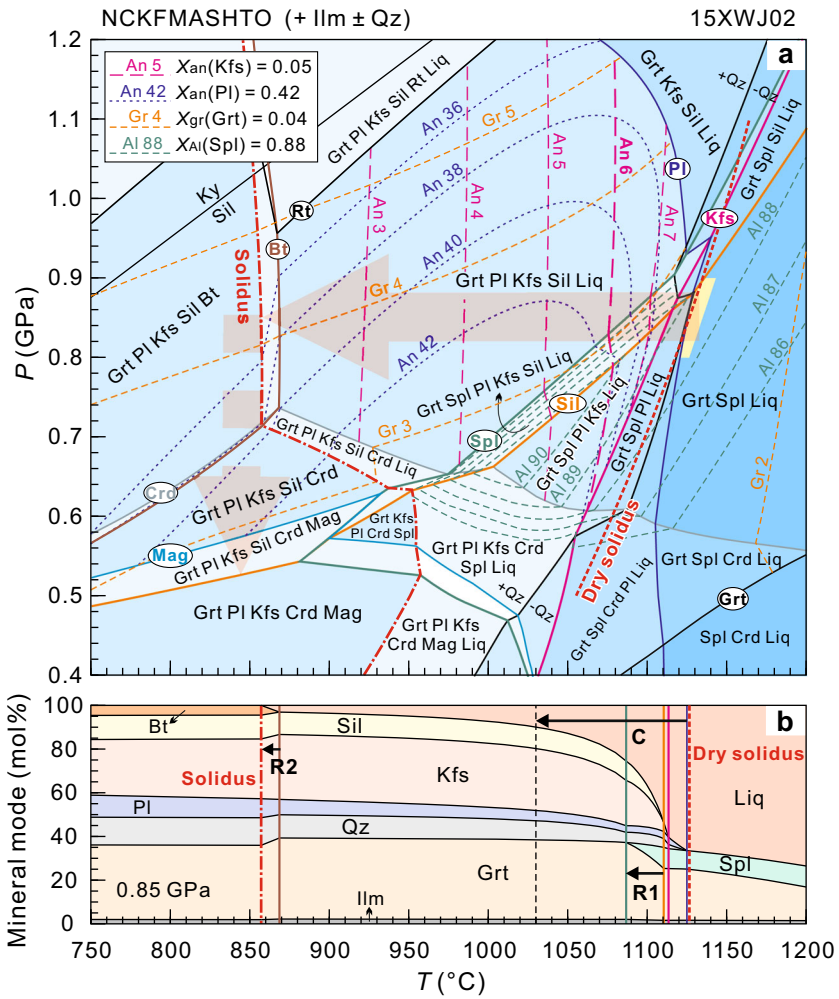

Fig. 6 **a** *P*–*T* pseudosection with proposed T_{max} conditions and *P*–*T* path for sample 15XWJ02. The compositional isopleths of spinel, garnet, K-feldspar and plagioclase are contoured in the relevant assemblages. The dry solidus was calculated in H_2O-free subsystem. **b** *T*–Mode diagram showing the variation of mineral and melt modes, and the temperature ranges of melt crystallization (C) and crucial metamorphic reactions (R1 and R2) along the cooling path at 0.85 GPa. Mineral abbreviations are after Whitney and Evans (2010). *Liq* = silicate melt

and a pressure range of 0.7–1.0 GPa. Moreover, the measured X_{an} in plagioclase of 0.40–0.42 from the inclusions in perthite and 0.38–0.39 from the matrix grains yield temperatures fairly consistent with the initial and later growth of plagioclase during cooling.

The symplectitic and coronary assemblages around garnet, sillimanite and biotite (Fig. 3a–g) indicate further evolution in sub-solidus conditions. These will be addressed below.

Spinel-involving equilibria

The bulk-rock composition of sample 15XWJ02 (Wang et al. 2019) is presented herein as Table 3. Normalized molar proportions of main constituents corresponding to Figs. 6–8 are presented in Table 4.

The phase equilibria modelling (Fig. 6) suggests that spinel should have been consumed through the reaction R1, and thereby could not survive as matrix grains during cooling to the fluid-absent solidus. Besides, the pseudosection in Fig. 6a cannot accommodate the higher X_{Al} of 0.90–0.95 and the wide variation of X_{Mg} in spinel (Fig. 4c). On these accounts, the $T-M(SiO_2)$, $T-X_{Fe}^{3+}$ and T–X_{Mg} pseudosections at 0.85 GPa (Figs. 7 and 8) were calculated to investigate how these components influence the stability and composition of spinel. In the $T-M(SiO_2)$ pseudosection (Fig. 7), spinel can stabilize to much lower temperatures and even down to sub-solidus conditions in the quartz-absent assemblages, suggesting that spinel can be preserved in local domains isolated from quartz. The X_{Al} values in spinel are predicted to roughly increase as temperature decreases above the solidus. The measured X_{Al} of 0.90–0.94 in the mantle of the zoned spinel can appear during the cooling evolution in the SiO_2-unsaturated fields (Fig. 7). Also suggested in Fig. 7, both the solidus and biotite growth can move to higher temperatures above 900 °C in SiO_2-unsaturated situations.

The $T-X_{Fe}^{3+}$ pseudosection (Fig. 8a) suggests that the spinel stability is slightly extended with increasing X_{Fe}^{3+}, and spinel is replaced by magnetite at $X_{Fe}^{3+} > 0.32$ fields. The X_{Al} values of spinel decrease dominantly with increasing X_{Fe}^{3+} and slightly with ascending temperature in the higher-T sillimanite-absent fields, while the spinel X_{Al} decreases dominantly with descending temperature and slightly with increasing X_{Fe}^{3+} in the lower-T sillimanite-present fields. The $T-X_{Mg}$ pseudosection (Fig. 8b) shows that the spinel stability is distinctly extended to lower temperatures with decreasing bulk-rock X_{Mg}, and spinel is replaced by magnetite in Fe-rich rocks with $X_{Mg} < 0.33$. The X_{Mg} values of spinel increase dominantly with increasing bulk-rock X_{Mg}, almost temperature independent in the higher-T sillimanite-absent assemblages, while in the lower-T sillimanite-present assemblages, the spinel X_{Mg} increases mainly with increasing temperature.

Monte Carlo simulation results

The cleaned zircon $^{207}Pb/^{206}Pb$ dates (174 data) distribute from 1887 ± 18 to 1954 ± 23 Ma, with a mean age of 1919 ± 2 Ma [mean squared weighted deviation (MSWD) = 1.19; Fig. 9a]. The frequency histogram with density estimate shows that these ages are within one group (Fig. 9b), which indicates a prolonged metamorphic event. The frequency histogram and cumulative probability curve as functions of the duration that were calculated from the resulting age differences are shown in Fig. 9c, d. The simulation results indicate that the duration was ~40 Myr (95% confidence).

Discussion

Metamorphic evolution

Petrographic characteristics and phase equilibria modelling of the spinel-bearing pelitic granulite sample from the Xuwujia area suggest a metamorphic evolution dominated by cooling from a T_{max} stage with extremely high temperatures of >1125 °C (at 0.8–0.9 GPa). This extreme condition is consistent with the occurrence of ferro-pseudobrookite, which indicates temperatures above 1120 °C as previously reported by Wang et al. (2019). The peak temperature is above the dry solidus of the rock, which may have resulted in over 60 mol% melts with only spinel and garnet survived (Fig. 6) even in the mesosomes of the migmatite.

The post-T_{max} cooling was inferred to proceed at pressures of 0.8–0.9 GPa from (i) the isopleths of the measured X_{an}(Pl) and X_{gr}(Grt) values, and (ii) the stability of the biotite-bearing and rutile-absent final assemblage in Fig. 6a. This pressure condition is consistent with the results from previous studies in the Jining complex (e.g. Jiao and Guo 2011; Li and Wei 2018; Li et al. 2019). The cooling process from the peak

Table 3 Bulk-rock chemical composition of sample 15XWJ02*

Constituent	SiO_2	TiO_2	Al_2O_3	Fe_2O_3	MnO	MgO	CaO	Na_2O	K_2O	P_2O_5	LOI	Total
Content (wt%)	52.6	0.85	21.47	12.13	0.08	5.32	1.26	1.38	3.68	0.02	0.93	99.72

LOI = loss on ignition

* Data from Wang et al. (2019)

Table 4 Normalised proportions (mol%) of sample 15XWJ02

Figure	H_2O^*	SiO_2	Al_2O_3	CaO	MgO	FeO_{total}	K_2O	Na_2O	TiO_2	O^*	X_{Fe}^{3+}	X_{Mg}
6	0.49	58.88	14.16	1.51	8.87	10.22	2.63	1.50	0.72	1.02	0.20	0.52
7	0.66	45.0	18.94	2.02	11.86	13.67	3.52	2.01	0.96	1.36		
	0.42	65.0	12.05	1.29	7.55	8.70	2.24	1.28	0.61	0.87		
8a	0.50	59.49	14.31	1.52	8.96	10.32	2.66	1.52	0.72	0	0	
	0.48	57.99	13.95	1.49	8.74	10.06	2.59	1.48	0.70	2.52	0.5	
8b	0.49	58.88	14.16	1.51	3.41	15.68	2.63	1.50	0.72	1.02		0.2
	0.49	58.88	14.16	1.51	11.93	7.16	2.63	1.50	0.72	1.02		0.7

$X_{Fe}^{3+} = Fe^{3+}/Fe = 2O/FeO_{total}$; $X_{Mg} = MgO/(MgO + FeO)$

* Adjusted proportions

temperature to the fluid-absent solidus involves three crucial retrograde metamorphic reactions (Fig. 6b), which are Liq = Kfs + Pl + Qz (C at 1030–1125 °C), Spl + Qz = Grt + Sil (R1 at 1085–1110 °C) and Grt + Kfs + Liq = Bt + Pl + Qz (R2 at 860–870 °C), corresponding to the successive appearance of plagioclase, K-feldspar, sillimanite and biotite. The temperature of R1 can well match that of the experimentally constrained univariant reaction (Fig. 10; Hensen 1986; Kelsey et al. 2004). The cooling evolution is also supported by (i) the exsolution of magnetite from spinel at 1000–1050 °C (Figs. 5; 10; Taylor-Jones and Powell 2010) and the formation of perthite from supra-solvus Ca-rich K-feldspar (Fig. 4f); (ii) the core-to-rim increasing X_{gr} in garnet (0.03 → 0.04; Figs. 4b and 6a) and increasing X_{Al} in spinel (0.87–0.88 → 0.94–0.95; Figs. 4c and 7); and (iii) the rutile needles exsolved from garnet (Fig. 3a) which indicates the expulsion of titanium from garnet through open system precipitation (e.g. Proyer et al. 2013).

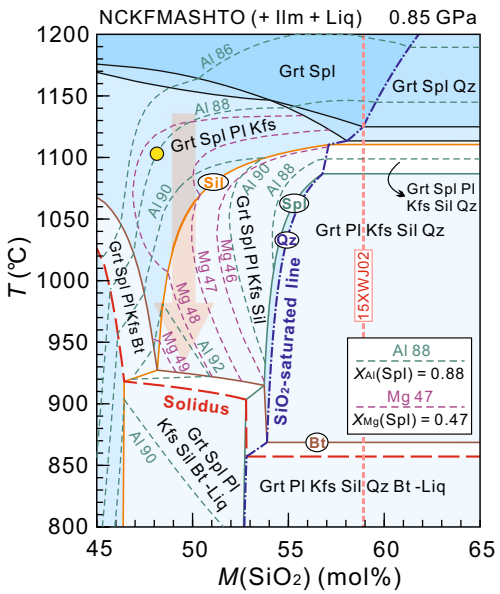

Fig. 7 T–$M(SiO_2)$ pseudosection calculated for sample 15XWJ02 at 0.85 GPa, showing the variation the phase relations, especially the stability of spinel, with the bulk-rock or local domain $M(SiO_2)$ values. Also shown are the compositional isopleths of spinel and the minimum temperature (solid circle) indicated by X_{Al} in the core of the zoned spinel

The post-T_{max} cooling evolution may terminate at the fluid-absent solidus and is followed by a sub-solidus decompression stage, indicated by the development of symplectitic or coronary Crd − Opx − Spl assemblages around garnet, sillimanite or biotite (Fig. 3a–g), as well as by the overgrowth of magnetite around ilmenite (Figs. 3h and 6a). The formation of the symplectitic or coronary assemblages can be attributed to the reactions governed by local domains, such as Grt + Sil = Crd + Spl and Grt + Bt = Crd + Opx, which may occur at 0.4–0.6 GPa (Fig. 10).

In addition, a pre-T_{max} heating decompression stage can be inferred from the spinel inclusions in the rim domain of garnet (Fig. 3a; Li et al. 2019) and the survival rutile inclusions (Figs. 3i and 6a). Such a pre-T_{max} evolution was also recovered from the UHT granulites at other outcrops in the Jining complex, such as Tuguiwula and Hongshaba (Li and Wei 2018; Li et al. 2019).

As a result, a clockwise P–T path can be recovered for the spinel-bearing granulite at the Xuwujia area. It involves the pre-T_{max} heating decompression to the T_{max} stage, the post-T_{max} cooling to fluid-absent solidus and the sub-solidus decompression (Fig. 10).

Timescale of the UHT metamorphism

Most of the previous zircon U–Pb dating data for UHT granulites from the Jining complex show wide and continuous age distributions on the concordia curve, with weighted mean ages of ~1.92 Ga (Santosh et al. 2007a; Li and Wei 2018; Lobjoie et al. 2018; Li et al. 2019). Nevertheless, the geological meaning of the mean value from a very wide age span is ambiguous, and the wide age span is likely ascribed to slow cooling of UHT granulites (e.g. Li and Wei 2016; Jiao et al. 2020; Laurent et al. 2018; Clark et al. 2018). Recently, Huang et al. (2019) reported that some zircon grains yield mean ages

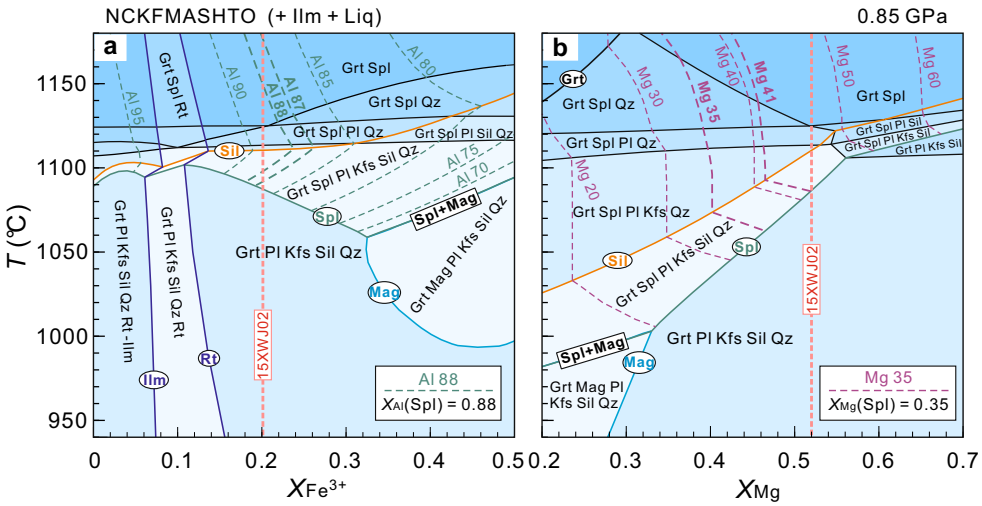

Fig. 8 T–X_{Fe}^{3+} (**a**) and T–X_{Mg} (**b**) pseudosections calculated for sample 15XWJ02 at 0.85 GPa, showing the variation of the stability and composition (X_{Al} and X_{Mg}) of spinel with the bulk-rock or local domain X_{Fe}^{3+} and X_{Mg} values. The dashed lines labeled with sample number represent the relevant values used in Fig. 6

of ~1.94 Ga in the cores and ~ 1.92 Ga in the rims, and interpreted that the ~1.94 Ga age represents the prograde anatexis predated UHT metamorphism and the ~1.92 Ga age represents later UHT metamorphism. However, Wang et al. (2020) performed texture constrained in-situ dating and revealed that zircon included in biotite yields an age of ~1.90 Ga and zircon included in sillimanite and perthite yields ages of ~1.94 Ga. Meanwhile, phase equilibria modelling shows that sillimanite and perthite have grown at 1010–1120 °C and biotite formed at ~900 °C both during cooling, so it suggests a supra-solidus cooling stage at 1.94–1.90 Ga (Wang et al. 2020). In this study, Monte Carlo simulative results suggest a duration of ~40 Myr (95% confidence; Fig. 9d). Considering that zirconium behaves as incompatible element and crystallization of melts and consequent growth of zircon generally occurs during post-peak cooling (e.g. Harley et al. 2007; Kelsey et al. 2008), we interpret this duration to represent a prolonged supra-solidus cooling stage during 1.94–1.90 Ga in the Jining complex. This timing is more meaningful for a regional metamorphic event and is accordant with that (i) the UHT metamorphism took place after the ~1.95 Ga high-pressure granulite facies metamorphism (e.g. Li and Wei 2018); (ii) the garnet-bearing granites were crystallized at ~1.92 Ga as the products of the UHT

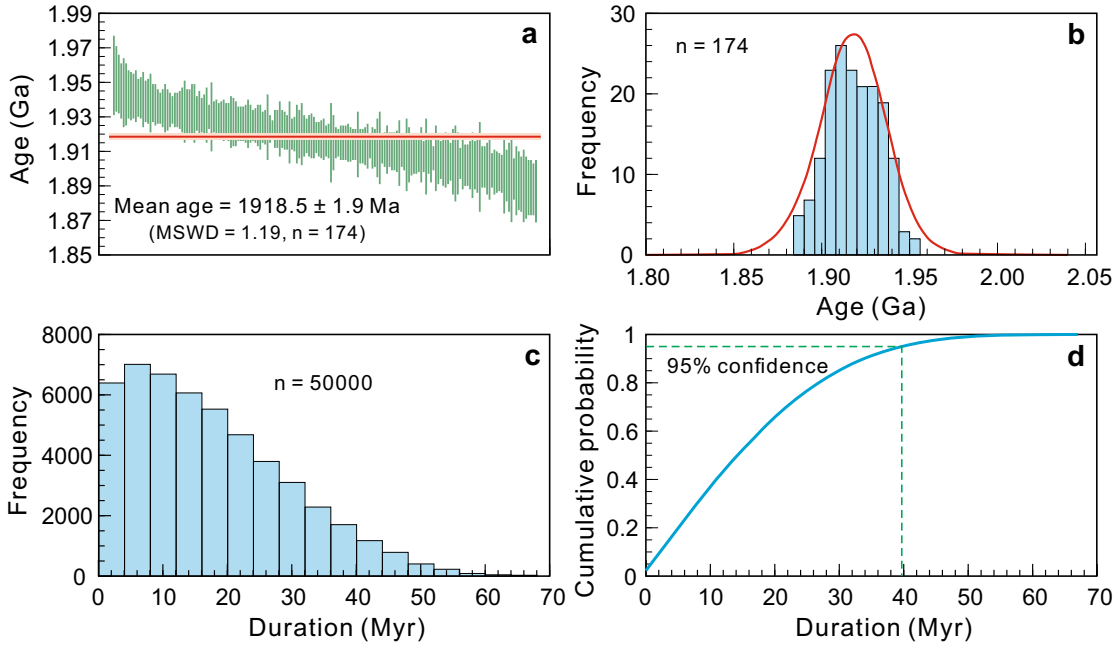

Fig. 9 Statistic and simulated results of zircon $^{207}Pb/^{206}Pb$ dates for the UHT granulites in the Jining complex. **a** Weighted mean age. **b** Frequency distribution of the measured age values. **c** Frequency distribution of the calculated durations. **d** Cumulative probability of the durations. The data of metamorphic zircon are collected from Santosh et al. (2007a), Yang et al. (2014), Li and Wei (2016, 2018), Lobjoie et al. (2018) and Li et al. (2019)

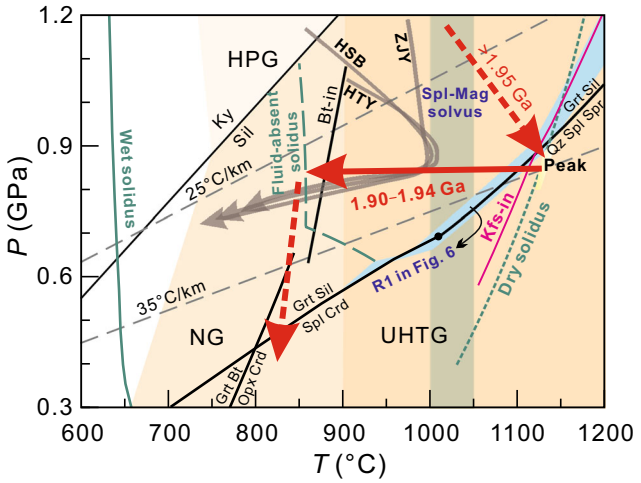

Fig. 10 *P–T* diagram showing the *P–T–t* evolution of the spinel-bearing UHT granulite at the Xuwujia area. Also shown are: (i) experimentally constrained crucial metamorphic reactions (solid curves; Hensen 1986; Kelsey et al. 2004; Stevens et al. 1997); (ii) the solvus of the spinel–magnetite suggested by the compatibility diagrams in Taylor-Jones and Powell (2010); and (iii) calculated dry solidus, fluid-absent solidus, K-feldspar-in (Kfs-in) line and the sliding reaction R1 in Fig. 6. The similar *P–T* paths with lower peak temperatures for UHT granulites at the nearby outcrops, involving Zhaojiayao (ZJY; Li and Wei 2016), Hongshaba (HSB; Li et al. 2019) and Huangtuyao (HTY; Liao and Wei 2019), are presented for comparison. The granite wet solidus was cited from Johannes and Holtz (1996). The *P–T* ranges for the metamorphic facies of normal granulite (NG), ultrahigh-temperature granulite (UHTG) and high-pressure granulite (HPG) were cited from Brown (2007)

metamorphism (Wang et al. 2018; Shi et al. 2018); and (iii) the gabbronorites emplacement at 1.96–1.92 Ga (Peng et al. 2010) were involved in the genesis of the UHT metamorphism (Guo et al. 2012; Li and Wei 2018; Wang et al. 2019; Huang et al. 2019).

Spinel behaviour

Like that in the studied sample, a considerable amount of spinel in the granulite can survive during cooling (Fig. 2b), although it is predicted to be consumed (Fig. 6). This is commonly interpreted by the involvement of ZnO in spinel (e.g. Yang et al. 2014; Li et al. 2019), which can enlarge the stability of spinel to lower temperatures (Sengupta et al. 1991; Nichols et al. 1992; Hand et al. 2007; Tajcmanová et al. 2009). Experimental calibration in Nichols et al. (1992) shows that an incremental X_{Zn} of 0.2 can contribute about −150 °C to the lower limit of spinel stability range. However, in the case of this study, the low X_{Zn} in spinel of 0.02–0.05 (Fig. 4d) is not enough to explain its preservation in the rock. Phase equilibria modelling suggests that spinel stability can be markedly enlarged in the local domains that are lower in SiO_2 or X_{Mg} (Figs. 7; 8b) due to the heterogeneous distribution of quartz or mafites in the rock. This is accordant with the observations that spinel commonly survives in local quartz-free domains (Tajcmanová et al. 2009) or is texturally isolated from quartz (Kelsey 2008).

The two key compositional variables (X_{Mg} and X_{Al}) of spinel are governed by both metamorphic temperatures and local domain compositions. For instance, the measured X_{Mg} of 0.35–0.41 in spinel as inclusions and matrix grains (Fig. 4c) may represent cooling temperatures below ~1090 °C at the local compositions with X_{Mg} around 0.4–0.5 (Fig. 8b), which is somewhat lower than the measured bulk-rock X_{Mg} of 0.52. This is consistent with that these spinel grains closely coexist with ilmenite (Fig. 3b, e). Besides, the measured higher X_{Mg} of 0.39–0.47 in the symplectitic spinel intergrown with cordierite should be primarily ascribed to the local Mg-rich domains, although these equilibria have not been presented in Fig. 8b. Similarly, the core-to-rim increasing X_{Al} and variation trend of X_{Mg} in the zoned spinel may indicate a temperature decrease at local domains isolated from quartz (Figs. 4c and 7), consistent with the recovered post-T_{max} cooling evolution of the rock. Therefore, the reintegrated X_{Al} of 0.87–0.88 from the spinel core with exsolved magnetite lamellae may represent temperatures over ~1100 °C (Fig. 7), seeing that spinel grains do not coexist with any biotite. By the way, it should be noted that the compositional zoning of spinel (Fig. 4c) corresponds to the spectacular textural zoning in form of exsolution (Fig. 5), which benefits to the composition restriction because the degree of openness for cations diffusion depends on the boundary conditions (e.g. Proyer et al. 2013).

The frequently observed coexistence of spinel and ilmenite (Fig. 3b–e) suggests that spinel has survived together with ilmenite as refractory residuum at peak temperatures. Calculation shows that the spinel can contain ulvöspinel (Fe_2TiO_4) up to ~3 mol% at the peak stage. However, the measured and even the reintegrated spinel composition did not contain any perceptible Ti and meanwhile, no ulvöspinel-rich phase (e.g. titanomagnetite) was found inside or around spinel. Therefore, the Ti-component should be preferentially expulsed from spinel, in the form of ilmenite, through open system precipitation (e.g. Proyer et al. 2013) during the initial cooling. This is consistent with that the ilmenite mode slightly increases at 1090–1110 °C (Fig. 6b).

Furthermore, as suggested by the orthogonal compatibility diagrams in Taylor-Jones and Powell (2010) and Wheller and Powell (2014), the solvus of the miscible spinel–magnetite phase locates between 1000 and 1050 °C and behaves almost pressure independent. Hence, spinel with exsolved lamellae of magnetite can be an indicator of UHT conditions in metapelites, likely for temperatures above 1000 °C.

Tectonic implications

The spinel-bearing UHT granulite at the Xuwujia area was revealed to evolve along a clockwise *P–T* path including the pre-T_{max} heating decompression, post-T_{max} cooling to the

fluid-absent solidus, and sub-solidus decompression stages (Fig. 10). The pre-T_{max} heating decompression may suggest an exhumation of the high-pressure granulite terrane, which was proposed to relate with an orogenic crustal thickening event at 1.98–1.96 Ga (Zhou et al. 2010; Li et al. 2011; Yin et al. 2011). The recovered T_{max} temperature is extremely high to ~1125 °C, located above the dry solidus of the investigated granulite (Fig. 10), which caused extensive crustal anatexis and generated the schlieren migmatite (Fig. 2a) and garnet-bearing granite in the field. The post-T_{max} cooling evolution occurred at a middle–lower crustal level (0.8–0.9 GPa) and lasted for ~40 Myr (1.94–1.90 Ga; Figs. 9 and 10).

The tectonic setting for the UHT metamorphism in the Jining complex was controversially proposed to be ridge subduction (e.g. Peng et al. 2010; Guo et al. 2012; Santosh et al. 2012) and post-collision mantle upwelling together with mafic magma emplacement (e.g. Zhao 2009; Li and Wei 2018). The ridge subduction scenario may not be favored on considerations that (i) it may involve the generation of paired metamorphic belts of high- and low-P/T types and adakitic rocks from oceanic slab melting (e.g. Iwamori 2000; Santosh and Kusky 2010), which have not yet been discovered in the region; and (ii) a ridge subduction triggered UHT metamorphism may occur at pressures over 2 GPa (Syracuse et al. 2010) and cool down within ~2 Myr (Iwamori 2000), which are distinct from the characters of the UHT metamorphism in the Jining complex. The model of post-collision mantle upwelling together with mafic magma emplacement seems also inappropriate because the UHT metamorphism in this scenario usually lasted somewhat shorter (mostly within 30 Myr; Harley 2016; Kelsey and Hand 2015) and has limited temperatures below ~1000 °C (Harley 2004). For instance, the HT–UHT metamorphic overprinting related to mantle upwelling resulted from delamination in the Bohemian massif shows limited temperatures (~900 °C) and short-lived duration (e.g. Faryad and Cuthbert 2020). The prolonged UHT metamorphism, such as that in the Xuwujia area, is generally regarded to be formed in the hot underbelly of an orogen with external heat source (e.g. Harley 2016). A thermal modelling suggests that a plume-induced hot mantle upwelling can result in efficient lithosphere thermal erosion and can conductively heat the overlying crust, which, however, cannot generate the extreme UHT metamorphism (>1100 °C) without the advective heating by massive magma penetrating the granulite terranes (Wang et al. 2019). This scenario is appropriate for the Xuwujia area, where the gabbronorites with crystallization ages of 1.96–1.92 Ga show a hyperthermal primary intrusive temperature of 1400 °C and an anomalously high mantle potential temperature of 1550 °C (Peng et al. 2010). Therefore, a post-orogenic mantle plume activity accompanied with the intrusion of mantle-derived magma is more possible to account for the UHT metamorphism in the Jining complex, where the extremely high temperatures (>1100 °C) may be reached with sufficient advective heating from hyperthermal intrusions at the Xuwujia and Tianpishan areas, while less heating may depress the temperatures at, for instance, the Zhaojiayao and Hongshaba areas (Figs. 1c and 10). In addition, the 1.94–1.90 Ga UHT metamorphism in the Jining complex, North China Craton is synchronous with the markedly global Orosirian (2.0–1.88 Ga) UHT metamorphic events (Brown 2007), such as those in the Lewisian complex, Scotland (e.g. Baba 2003; Hollis et al. 2006) and the Taltson zone, northwestern Canada (Farquhar et al. 1996).

Acknowledgements We thank Xiaoli Li for his assistance with experimentation. We appreciate the constructive comments and suggestions from reviews Alexander Proyer and Martin Racek and the thorough editorial work of editors Shah Wali Faryad and Lutz Nasdala. The present study was financially supported by the National Natural Science Foundation of China (grants 42030304 and 4189083013).

References

Ague JJ, Eckert JO (2012) Precipitation of rutile and ilmenite needles in garnet: implications for extreme metamorphic conditions in the Acadian Orogen, USA. Am Mineral 97:840–855

Baba S (2003) Two stages of sapphirine formation during prograde and retrograde metamorphism in the Paleoproterozoic Lewisian complex in South Harris, NW Scotland. J Petrol 44:329–354

Brown M (2007) Metamorphic conditions in orogenic belts: a record of secular change. Int Geol Rev 49:193–234

Clark C, Taylor RJM, Kylander-Clark ARC, Hacker BR (2018) Prolonged (>100 Ma) ultrahigh temperature metamorphism in the Napier complex, East Antarctica: a petrochronological investigation of Earth's hottest crust. J Metamorph Geol 36:1117–1139

Clarke GL, Powell R, Guiraud M (1989) Low-pressure granulite facies metapelitic assemblages and corona textures from MacRobertson land, East Antarctica: the importance of Fe_2O_3 and TiO_2 in accounting for spinel-bearing assemblages. J Metamorph Geol 7:323–335

Das E, Karmakar S, Dey A, Karmakar S, Sengupta P (2017) Reaction textures, pressure-temperature paths and chemical dates of monazite from a new suite of sapphirine-spinel granulites from parts of the eastern Ghats Province, India: insights into the final amalgamation of India and East Antarctica during the formation of Rodinia. In: Pant NC, Dasgupta S (eds) Crustal evolution of India and Antarctica: the supercontinent connection, vol 457. Geol Soc Lond Spec Publ, pp 141–170

Elkins LT, Grove TL (1990) Ternary feldspar experiments and thermodynamic models. Am Mineral 75:544–559

Farquhar J, Chacko T, Ellis DJ (1996) Preservation of oxygen isotope compositions in granulites from northwestern Canada and Enderby Land, Antarctica: implications for high-temperature isotopic thermometry. Contrib Mineral Petrol 125:213–224

Faryad SW, Cuthbert SJ (2020) High-temperature overprint in (U)HPM rocks exhumed from subduction zones: a product of isothermal decompression or a consequence of slab break-off (slab rollback)? Earth-Sci Rev 202:103108

Guiraud M, Kienast J, Rahmani A (1996) Petrological study of high-temperature granulites from in Ouzzal, Algeria: some implications on the phase relationships in the FMASTOCr systems. Eur J Mineral 8:1375–1390

Guo JH, Shi X, Bian A, Xu R, Zhai MG, Li Y (1999) Pb isotopic composition of feldspar and U–Pb age of zircon from early Proterozoic

granite in Sanggan area, North China Craton: metamorphism, crustal melting and tectono-thermal event. Acta Petrol Sin 15:199–207 (in Chinese with English abstract)

Guo JH, Peng P, Chen Y, Jiao SJ, Windley BF (2012) UHT sapphirine granulite metamorphism at 1.93–1.92 Ga caused by gabbronorite intrusions: implications for tectonic evolution of the northern margin of the North China Craton. Precambrian Res 222–223:124–142

Hand M, Scrimgeour I, Powell R, Stüwe K, Wilson CJL (2007) Metapelitic granulites from Jetty peninsula, East Antarctica: formation during a single event or by polymetamorphism. J Metamorph Geol 12:557–573

Harley SL (2004) Extending our understanding of ultrahigh temperature crustal metamorphism. J Mineral Petrol Sci 99:140–158

Harley SL (2008) Refining the P–T records of UHT crustal metamorphism. J Metamorph Geol 26:125–154

Harley SL (2016) A matter of time: the importance of the duration of UHT metamorphism. J Mineral Petrol Sci 111:50–72

Harley SL, Kelly NM, Moller A (2007) Zircon behaviour and the thermal histories of mountain chains. Elements 3:25–30

Hensen BJ (1986) Theoretical phase relations involving cordierite and garnet revisited: the influence of oxygen fugacity on the stability of sapphirine and spinel in the system mg-Fe-Al-Si-O. Contrib Mineral Petrol 92:362–367

Holland TJB, Powell R (2011) An improved and extended internally-consistent thermodynamic dataset for phases of petrological interest, involving a new equation of state for solids. J Metamorph Geol 29: 333–383

Hollis JA, Harley SL, White RW, Clarke GL (2006) Preservation of evidence for prograde metamorphism in UHT-HP granulites, South Harris, Scotland. J Metamorph Geol 24:263–279

Huang GY, Guo JH, Jiao SJ, Palin RM (2019) What drives the continental crust to be extremely hot so quickly. J Geophys Res Solid Earth 124:11218–11231

Iwamori H (2000) Thermal effects of ridge subduction and its implications for the origin of granitic batholiths and paired metamorphic belts. Earth Planet Sci Lett 181:131–144

Jiao SJ, Guo JH (2011) Application of the two-feldspar geothermometer to ultrahigh-temperature (UHT) rocks in the Khondalite Belt, North China Craton and its implications. Am Mineral 96:250–260

Jiao SJ, Guo JH, Evans NJ, Mcdonald BJ, Liu P, Ouyang DJ, Fitzsimons ICW (2020) The timing and duration of high-temperature to ultrahigh-temperature metamorphism constrained by zircon U–Pb–Hf and trace element signatures in the Khondalite Belt, North China Craton. Contrib Mineral Petrol 175:66

Johannes W, Holtz F (1996) Petrogenesis and experimental petrology of granitic rocks. In: El Goresy A, von Engelhardt W, Hahn T (eds) Minerals and rocks. Springer Verlag, Berlin, p 271

Kelsey DE (2008) On ultrahigh-temperature crustal metamorphism. Gondwana Res 13:1–29

Kelsey DE, Hand M (2015) On ultrahigh temperature crustal metamorphism: phase equilibria, trace element thermometry, bulk composition, heat sources, timescales and tectonic settings. Geosci Front 6: 311–356

Kelsey DE, White RW, Holland TJB, Powell R (2004) Calculated phase equilibria in K_2O-FeO-MgO-Al_2O_3-SiO_2-H_2O for sapphirine-quartz-bearing mineral assemblages. J Metamorph Geol 22:559–578

Kelsey DE, Clark C, Hand M (2008) Thermobarometric modelling of zircon and monazite growth in melt bearing systems: examples using model metapelitic and metapsammitic granulites. J Metamorph Geol 26:199–212

Korhonen FJ, Saw AK, Clark C, Brown M, Bhattacharya S (2011) New constraints on UHT metamorphism in the eastern Ghats Province through the application of phase equilibria modelling and in situ geochronology. Gondwana Res 20:764–781

Korhonen FJ, Powell R, Stout JH (2012) Stability of sapphirine plus quartz in the oxidized rocks of the Wilson Lake terrane, Labrador: calculated equilibria in NCKFMASHTO. J Metamorph Geol 30:21–36

Laurent AT, Bingen B, Duchene S, Whitehouse MJ, Seydoux-Guillaume AM, Bosse V (2018) Decoding a protracted zircon geochronological record in ultrahigh temperature granulite, and persistence of partial melting in the crust, Rogaland, Norway. Contrib Mineral Petrol 173:29

Li XW (2019) Paleoproterozoic ultrahigh temperature metamorphism in the Jining region, Khondalite Belt, North China Craton. Doctoral dissertation, Peking University, Beijing

Li XW, Wei CJ (2016) Phase equilibria modelling and zircon age dating of pelitic granulites in Zhaojiayao, from the Jining Group of the Khondalite Belt, North China Craton. J Metamorph Geol 34:595–615

Li XW, Wei CJ (2018) Ultrahigh-temperature metamorphism in the Tuguiwula area, Khondalite Belt, North China Craton. J Metamorph Geol 36:489–509

Li XP, Yang ZY, Zhao GC, Grapes R, Guo JH (2011) Geochronology of khondalite-series rocks of the Jining complex: confirmation of depositional age and tectonometamorphic evolution of the North China Craton. Int Geol Rev 53:1194–1211

Li XL, Zhang LF, Wei CJ, Slabunov AI, Bader T (2018) Quartz and orthopyroxene exsolution lamellae in clinopyroxene and the metamorphic P-T path of Belomorian eclogites. J Metamorph Geol 36: 11–12

Li XW, White RW, Wei CJ (2019) Can we extract ultrahigh-temperature conditions from Fe-rich metapelites? An example from the Khondalite Belt, North China Craton. Lithos 328–329:228–243

Liao Y, Wei CJ (2019) Ultrahigh-temperature mafic granulite in the Huai'an complex, North China Craton: evidence from phase equilibria modelling and amphibole thermometers. Gondwana Res 76: 62–76

Liu SJ, Li JH (2007) Review of ultrahigh-temperature (UHT) metamorphism study: a case from North China Craton. Geosci Front 14:131–137

Liu SJ, Xiang B, Li JH, Santosh M (2011) Retrograde metamorphism of ultrahigh-temperature granulites from the Khondalite belt in Inner Mongolia, North China Craton: evidence from aluminous orthopyroxenes. Geo J 46:263–275

Liu SJ, Tsunogae T, Li WS, Shimizu H, Santosh M, Wan YS, Li JH (2012) Paleoproterozoic granulites from Heling'er: implications for regional ultrahigh-temperature metamorphism in the North China Craton. Lithos 148:54–70

Lobjoie C, Wei L, Trap P, Goncalves P, Li Q, Marquer D, Devoir A (2018) Ultra-high temperature metamorphism recorded in Fe-rich olivine-bearing migmatite from the Khondalite belt, North China Craton. J Metamorph Geol 36:343–368

Nichols GT, Berry RF, Green DH (1992) Internally consistent gahnitic spinel–cordierite–garnet equilibria in the FMASHZn system: Geothermobarometry and applications. Contrib Mineral Petrol 111:362–377

Peng P, Guo JH, Zhai MG, Bleeker W (2010) Paleoproterozoic gabbronoritic and granitic magmatism in the northern margin of the North China craton: evidence of crust–mantle interaction. Precambrian Res 183:635–659

Pouchou JL, Pichoir F (1985) "PAP" (phi-rho-Z) procedure for improved quantitative microanalysis. In: Armstrong JT (ed) Microbeam analysis. San Francisco Press, San Francisco, pp 104–106

Powell R, Holland TJB (1988) An internally consistent dataset with uncertainties and correlations: applications to geobarometry, worked examples and a computer program. J Metamorph Geol 6:173–204

Proyer A, Habler G, Abart R, Wirth R, Krenn K, Hoinkes G (2013) TiO_2 exsolution from garnet by open-system precipitation: evidence from

crystallographic and shape preferred orientation of rutile inclusions. Contrib Mineral Petrol 166:211–234

Santosh M, Kusky T (2010) Origin of paired high pressure–ultrahigh-temperature orogens: a ridge subduction and slab window model. Terra Nova 22:35–42

Santosh M, Wilde SA, Li JH (2007a) Timing of Paleoproterozoic ultrahigh-temperature metamorphism in the North China craton: evidence from SHRIMP U-Pb zircon geochronology. Precambrian Res 159:178–196

Santosh M, Tsunogae T, Li JH, Liu SJ (2007b) Discovery of sapphirine-bearing mg–Al granulites in the North China Craton: implications for Paleoproterozoic ultrahigh temperature metamorphism. Gondwana Res 11:263–285

Santosh M, Sajeev K, Li JH, Liu SJ, Itaya T (2009) Counterclockwise exhumation of a hot orogen: the Paleoproterozoic ultrahigh-temperature granulites in the North China Craton. Lithos 110:140–152

Santosh M, Liu SJ, Tsunogae T, Li JH (2012) Paleoproterozoic ultrahigh-temperature granulites in the North China Craton: implications for tectonic models on extreme crustal metamorphism. Precambrian Res 223:77–106

Sengupta P, Karmakar S, Dasgupta S, Fukuoka M (1991) Petrology of spinel granulites from Araku, eastern Ghats, India, and a petrogenetic grid for sapphirine-free rocks in the system FMAS. J Metamorph Geol 9:451–459

Sengupta P, Sen J, Dasgupta S, Raith M, Bhui UK, Ehl J (1999) Ultrahigh temperature metamorphism of metapelitic granulites from Kondapalle, eastern Ghats belt: implications for the indo-Antarctic correlation. J Petrol 40:1065–1087

Shi Q, Dong XJ, Xu ZY, Guan QB, Li PC, Zhang C, Cui FH (2018) Anatectic origin and geological significance of the Paleoproterozoic gneissic garnet granite in the Jining area, northern margin of the North China Craton. Acta Petrol Sin 34:2754–2772 (in Chinese with English abstract)

Shimizu H, Tsunogae T, Santosh M, Liu SJ, Li JH (2013) Phase equilibrium modelling of Palaeoproterozoic ultrahigh temperature sapphirine granulite from the Inner Mongolia suture zone, North China Craton: implications for counterclockwise P–T path. Geol J 48: 456–466

Stevens G, Clemens JD, Droop GTR (1997) Melt production during granulite facies anatexis: experimental data from "primitive" metasedimentary protoliths. Contrib Mineral Petrol 128:352–370

Svensen H, Corfu F, Polteau S, Hammer O, Planke S (2012) Rapid magma emplacement in the Karoo large Igneous Province. Earth Planet Sci Lett 325−326:1–9

Syracuse EM, Keken PEV, Abers GA (2010) The global range of subduction zone thermal models. Phys Earth Planet Inter 183:73–90

Tajcmanová L, Konopásek J, Kosler J (2009) Distribution of zinc and its role in the stabilization of spinel in high-grade felsic rocks of the Moldanubian domain (bohemian massif). Eur J Mineral 21:407–418

Taylor-Jones K, Powell R (2010) The stability of sapphirine + quartz: calculated phase equilibria in FeO–MgO–Al_2O_3–SiO_2–TiO_2–O. J Metamorph Geol 28:615–633

Wang W, Liu X, Hu J, Li Z, Zhao Y, Zhai MG, Liu XC, Clarke G, Zhang SH, Qu H (2014) Late Paleoproterozoic medium-P high grade metamorphism of basement rocks beneath the northern margin of the Ordos Basin, NW China: petrology, phase equilibrium modelling and U-Pb geochronology. Precambrian Res 251:181–196

Wang W, Gao S, Liu XC, Zhao Y, Wei CJ, Xiao W, Gong W (2017) Prolonged anatexis of Paleoproterozoic metasedimentary basement: first evidence from the Yinchuan Basin and new constraints on the evolution of the Khondalite Belt, North China Craton. Precambrian Res 302:74–93

Wang LJ, Guo JH, Yin CQ, Peng P, Zhang J, Spencer CJ, Qian JH (2018) High-temperature S-type granitoids (charnockites) in the Jining complex, North China Craton: Restite entrainment and hybridization with mafic magma. Lithos 320–321:435–453

Wang B, Tian W, Wei CJ, Di YK (2019) Ultrahigh metamorphic temperatures over 1050 °C recorded by Fe-Ti oxides and implications for Paleoproterozoic magma-induced crustal thermal perturbation in Jining area, North China Craton. Lithos 348–349:105180

Wang B, Wei CJ, Tian W, Fu B (2020) UHT metamorphism peaking above 1100 °C with slow cooling: insights from pelitic granulites in the Jining complex, North China Craton. J Petrol 61:egaa070

Waters DJ (1991) Hercynite–quartz granulites: phase relations, and implications for crustal processes. Eur J Mineral 3:367–386

Wheller CJ, Powell R (2014) A new thermodynamic model for sapphirine: calculated phase equilibria in K_2O–FeO–MgO–Al_2O_3–SiO_2–H_2O–TiO_2–Fe_2O_3. J Metamorph Geol 32:287–299

White RW, Powell R, Holland TJB, Johnson TE, Green ECR (2014) New mineral activity–composition relations for thermodynamic calculations in metapelitic systems. J Metamorph Geol 32:261–286

Whitney DL, Evans BW (2010) Abbreviations for names of rock-forming minerals. Am Mineral 95:185–187

Yang QY, Santosh M, Tsunogae T (2014) Ultrahigh-temperature metamorphism under isobaric heating: new evidence from the North China Craton. J Asian Earth Sci 95:2–16

Yin CQ, Zhao GC, Guo JH, Sun M, Xia X, Zhou X, Liu C (2011) U-Pb and Hf isotopic study of zircons of the Helanshan complex: constrains on the evolution of the Khondalite Belt in the Western block of the North China Craton. Lithos 122:25–38

Zhai MG, Santosh M (2011) The early Precambrian odyssey of the North China Craton: a synoptic overview. Gondwana Res 20:6–25

Zhang HT, Li JH, Liu SJ, Li WS, Santosh M, Wang HH (2012) Spinel + quartz-bearing ultrahigh-temperature granulites from Xumayao, Inner Mongolia suture zone, North China Craton: petrology, phase equilibria and counterclockwise P-T path. Geosci Front 3:603–611

Zhao GC (2009) Metamorphic evolution of major tectonic units in the basement of the North China Craton: key issues and discussion. Acta Petrol Sin 25:1772–1792 (in Chinese with English abstract)

Zhao GC, Sun M, Wilde SA, Li SZ (2005) Late Archean to Paleoproterozoic evolution of the North China Craton: key issues revisited. Precambrian Res 136:177–202

Zhao GC, Cawood PA, Li SZ, Wilde SA, Sun M, Zhang J, Yin CQ (2012) Amalgamation of the North China Craton: key issues and discussion. Precambrian Res 222:55–76

Zhong CT, Deng JF, Wan YS (2007) Magma recording of Paleoproterozoic orogeny in central segment of northern margin of North China Craton: geochemical characteristics and zircon shrimp dating of s-type granitoids. Geochimica 36:585–600

Zhou XW, Zhao GC, Geng YS (2010) Helanshan high pressure pelitic granulite: petrologic evidence for collision event in the western block of the North China Craton. Acta Petrol Sin 26:2113–2121 (in Chinese with English abstract)

Zhou LG, Zhai MG, Lu JS, Zhao L, Wang HZ, Wu JL, Liu B, Zou Y, Shan HX, Cui XH (2017) Paleoproterozoic metamorphism of high-grade granulite facies rocks in the North China Craton: study advances, questions and new issues. Precambrian Res 303:520–547